Computational analysis of chemomechanical behaviors of composite electrodes in Li-ion batteries

Rong Xu, Luize Scalco de Vasconcelos, and Kejie Zhao[a]
School of Mechanical Engineering, Purdue University, West Lafayette, IN 47906, USA

Mechanical reliability is a critical issue in all forms of energy conversion, storage, and harvesting. In Li-ion batteries, mechanical degradation caused by the repetitive swelling and shrinking of electrodes upon lithiation cycles is now well recognized; however, the impact of mechanical stresses on Li transport and hence the capacity of batteries is less obvious and underestimated. In particular, the stress field within the heterogeneous electrodes is complex, making the characterization of the chemomechanical behaviors of electrodes a challenging task. We develop a finite element program that computes the coupled Li diffusion and stresses in three-dimensional composite electrodes. We employ the reconstructed models of both cathode and anode materials to investigate the mechanical interactions of the constituents and their influence on the accessible capacity. The state of charge in the percolated particles is highly inhomogeneous regulated by the stress field. An ample space of design is open for the optimization of the capacity and mechanical performance of electrodes by tuning the size, shape, and pattern of active particles, as well as the properties of the inactive matrix.

I. INTRODUCTION

Li-ion batteries are the major power source in portable electronics and electric vehicles.[1,2] Innovation in the battery technology has been driven by the imperative demand of materials of light weight, high energy density, fast charging, long lifespan, and low cost.[3–5] Mechanical degradation of batteries caused by the repetitive swelling and shrinking of electrodes in the lithiation cycles is now well recognized.[6,7] The stress induced structural disintegration impedes electron conduction and causes persistent loss of capacity of batteries in the long-term cycles. In particular, the mechanical failure has become the bottleneck in the commercialization of high-capacity electrodes because of the massive volumetric deformation associated with the electrochemical processes. Figure 1 gives a brief survey of the volumetric strain of different types of cathode and anode materials. It is evident that drastic deformation is inherent to the high-capacity electrodes, such as S cathode as well as conversion and insertion type anodes.[8–12] The repetitive volumetric change in the active materials generates a complex field of stresses in the electrodes and leads to various sources of mechanical degradation including fracture,[13–17] plasticity,[18–20] and cavitation.[21,22]

While mechanical failure of batteries is frequently observed, less understood is the impact of stresses on the electrochemical processes, that is, how the locally generated stresses modify the energy landscape and kinetics of Li transport, interfacial reactions, and hence the capacity and potential of batteries.[23–26] Developing continuum models and numerical methods for the coupled Li diffusion and large deformation has been a topic of intense interests in the past few years, especially for the application of Si anode.[27–40] Nevertheless, most of prior research has been focused on idealized structures of single, isolated particles or two-dimensional structures. In commercial batteries, both the cathode and anode are composites of high heterogeneity at the nano- to microscale. A composite electrode is usually consisted of active particles of different sizes and irregular shapes, a matrix composed of polymer binders and additives, and pores filled with the electrolyte.[3,41] The components intimately interact with each other during the lithiation cycles and raise a complex field of stresses within the electrodes. Although the simplified models of single particles are useful to capture the first-order coupling effect between diffusion and stresses, the predictions on Li concentrations, stress field, and mechanical failure from the idealized models can be substantially different from that of the composite configurations. Relying on the techniques of x-ray tomographic microscopy and focused ion beam scanning electron microscope (FIB/SEM), the microstructure of composite electrodes in commercial batteries can be reconstructed with sufficient details and imported into
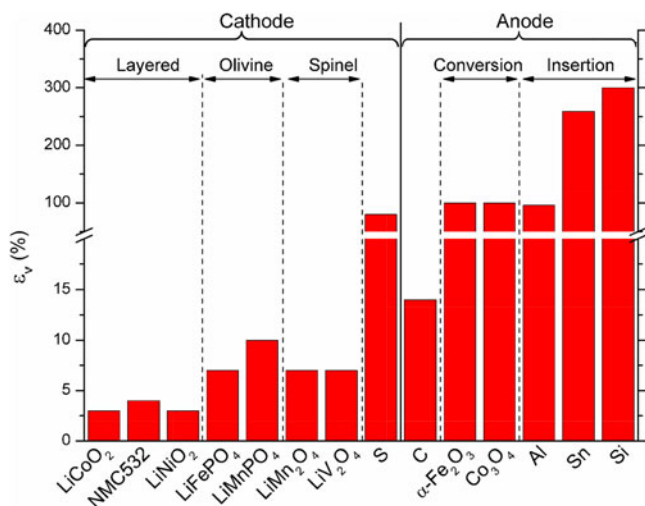

FIG. 1. A survey of volumetric strain of different types of cathode and anode materials.

the computational programs such as finite element methods (FEM) and finite volume methods (FVM).[42–44] Several groups have recently utilized the reconstructed 3D models to simulate the stress generation and electrochemical behaviors in more realistic configurations. The major findings, in comparison with the single-particle models, are as follows. (i) The stress field, Li concentration, and mechanical failure are strongly affected by the local details of the microstructure. (ii) The percolated bicontinuous network of reconstructed particles show significantly higher stresses than that in single isolated particles. (iii) The mechanical properties of binders, particularly the yield stress and elastic modulus, play an important role in determining the average stresses developed in the electrodes.[45–49]

In this paper, we reconstruct 3D composite models of $LiNi_{1/3}Mn_{1/3}Co_{1/3}O_2$ (NMC333, simplified as NMC in the following text) cathode and SnO anode based on extensive x-ray tomographic microscopy data. We implement the models into a developed finite element program that computes the coupled Li diffusion and stresses. We investigate the evolution of the stress field and the mechanical interactions regulated Li distribution and capacity of the electrodes. The state of charge in the active particles is highly inhomogeneous depending on the distribution of the percolated active particles and properties of the matrix. The effective capacity is limited by the inhomogeneous storage of Li and significant capacity loss is possible due to the particles contact and mechanical confinement of the surrounding medium. A map of the specific capacity of the composite electrodes in terms of the volume fraction and volumetric strain of the active particles is constructed. We anticipate an ample space of optimization on the capacity and mechanical performance of electrodes through tuning

the size, shape, and pattern of the active particles, as well as the stiffness, geometry, and porosity of the matrix.

II. THEORY AND FINITE ELEMENT MODELING

We consider the composite electrodes composed of two general components, active particles which store Li and inactive matrix which provides mechanical confinement to the deformation of the active materials. The inactive matrix is a representation of the effective medium including the polymer binders, conductive agents, and porosity in commercial batteries. The kinetics in batteries is often limited by Li diffusion in the active materials while Li transport through the porous matrix is usually a faster process. Here we consider that Li diffusion only occurs in the active material.

The continuum theory of coupled diffusion and large elasto-plasticity is described in a previous work[50] and its implementation into the finite element program is introduced in a recent publication.[51] In brevity, the displacement field in the active material is governed by the equation of mechanical equilibrium, $\nabla S + F_b = 0$, where S is the nominal stress calculated as $S = K : \varepsilon_e$, K the stiffness matrix, ε_e the elastic strain, and F_b the body force. The total deformation of a representative material element follows the kinematic multiplicative decomposition $F = F_e F_l F_p$, where F represents the deformation gradient, F_e the reversible elastic distortion of the material, F_l lithiation-induced volumetric deformation, and F_p the irreversible plastic deformation that dictates the shape change of the body. The elastic strain is computed as $\varepsilon_e = \frac{1}{2}\left(F_e^T F_e - I\right)$. The volumetric change due to Li insertion is $1 + \Omega C$, where Ω and C are the partial molar volume and concentration of Li, respectively. The material element yields under the von Mises conditions and the plastic deformation follows the J_2 flow theory. For the inactive material, the deformation and stresses are caused by the mechanical interactions with the active material. Its constitutive behavior is described by a Neo–Hookean model.[52] Traction-free and fixed boundary conditions are prescribed in the out-of-plane and in-plane directions, respectively, to model the film geometry of electrodes in commercial batteries. Li concentration is calculated by $\frac{\partial C}{\partial t} + \nabla J = 0$, where J is the nominal flux of Li, and ∇ represents the gradient with respect to the Lagrangian coordinate. Li flux is driven by the chemical potential μ, and can be written as $J = -\frac{CD}{kT}F^{-1}F^{-T}\nabla\mu$ following the standard transformation rules of continuum mechanics. The coupling of diffusion and stresses is represented in the form of the chemical potential of Li, $\mu = \mu_0 + kT \log\left(\frac{\gamma\Omega C}{\det(F)}\right) - \Omega\sigma_m$, where μ_0 is a reference value and γ the activity coefficients. The first two terms are the familiar expressions of the chemical potential for a species in nonideal solution,

and the third term represents the elastic energy change in isotropic materials upon insertion of guest species under stress, where $\sigma_m = \sigma_{kk}/3$ is the mean stress. A general formula accounting for the stress-dependent chemical potential in anisotropic solid solutions can be found in the work of Larché and Cahn.[53] For the diffusion boundary condition, we assume good ionic and electronic conductivities of the inactive materials such that each active particle experiences the same current or potential on the outer surface. In the reference state, the electrode is free of Li and stress. Lithiation is induced by imposing a galvanostatic or potentiostatic condition to the active particles. For galvanostatic lithiation, a constant nominal flux J_0 is prescribed. For potentiostatic lithiation, a constant chemical potential of Li μ_S is specified on outer surface of active particles. The idealized boundary conditions do not account for the kinetics of surface charge transfer at the interface of the electrode and electrolyte and exclude the nonuniform current density that a composite electrode may experience at various locations.[30,34,54,55]

The governing equations for the kinematics of deformation and the kinetics of diffusion are both strongly nonlinear. We integrate their weak formulations into the finite element program within a Lagrangian setting. The coupled equations for stress equilibrium and Li diffusion are solved simultaneously at every time step. The weak formulation for the force balance is obtained by following a standard procedure in continuum mechanics[51,56]:

$$\int_\Omega S\nabla v \, d\Omega - \int_\Omega F_b v \, d\Omega - \int_{\partial\Omega} P v \, dS = 0 \quad , \quad (1)$$

where $v(X_i, t)$ is a test function that vanishes on the boundary, and P represents the surface traction. For Li diffusion, the weak formulation is obtained by following the diffusion kinetics and by including the stress contribution to the Li chemical potential:

$$\int_\Omega \left(\frac{\partial C}{\partial t} \hat{\mu} - J\nabla\hat{\mu} \right) dV + \int_{\partial\Omega} (NJ)\hat{\mu} \, dS = 0 \quad . \quad (2)$$

The weak form Eq. (2) suggests that the chemical potential $\mu(X_i, t)$ is used as the field variable for Li transport, instead of the use of the nominal concentration $C(X_i, t)$. The true Li concentration c can be computed from the chemical potential and the mean stress σ_m by $c = \exp\{(\mu - \mu_0 + \Omega\sigma_m)/kT\}/\Omega$ and the nominal concentration is calculated by $C = c \det(F)$. Such a choice is beneficial for the numerical convergence. The weak formulations are implemented into the commercial software COMSOL Multiphysics™ (COMSOL 4.4, Sweden). The built-in time-dependent solver MUMPS (MUltifrontal Massively Parallel sparse direct Solver) is used to solve the co-evolution of Li concentration and stresses.[57] To improve the convergence, the segregated approach is adopted.

III. RECONSTRUCTION OF 3D COMPOSITE ELECTRODES AND STATISTICAL ANALYSIS

We reconstruct the microstructure of NMC cathode and SnO anode from experimentally segmented images and implement the reconstructed geometries into the finite element computational program. The 2D binarized images for the NMC and SnO electrodes are generously provided by Dr. Martin Ebner from the Wood group at ETH Zurich, who obtained these images using the synchrotron radiation x-ray tomographic microscopy technique. Interested readers may be referred to the open-source database hosted by ETH Zurich which provides the microstructural data for 16 different NMC-based electrodes with various degrees of compositions and morphologies.[58,59] We compile the 2D binarized images into Avizo 8.1 (FEI; Hillsboro, OR) to generate the 3D voxel data set in which the active particles and the inactive matrix are separately defined. Replying on the 3D voxel representation, a surface description (surface mesh with triangular grid) for both active particles and inactive matrix can be created in Avizo. Default surface meshes are often far too fine for the subsequent operations; we simplify the surface mesh and correct the major blemishes, such as triangles with poor aspect ratios, intersections, or acute dihedral angles of the surface mesh, using Avizo's surface editor. Then we generate a volumetric tetrahedral grid based on the previously created triangular surfaces. The tetrahedral grid mesh is the basis for producing different geometries of the electrode microstructure including the boundary, edges, and points, etc. Finally we employ the open-source tool MeshLab to smooth the volumetric tetrahedral grid using the Laplacian Smoothing Filter, and export the smoothed tetrahedral grid mesh in a Standard Tessellation Language (STL) file format that can be imported into the geometry module of COMSOL. The build-in mathematical models in COMSOL are applied to the reconstructed domains.

Figures 2(a)–2(c) show the active spheroidal NMC particles, the inactive matrix, and the reconstructed NMC electrode, respectively. The NMC electrode is reconstructed by a stack of 8-bit black and white binarized images of 889×889 pixels in which each of pixel size is 0.37 μm. The total volume of the reconstructed electrode is $329 \times 329 \times 74$ μm³. Statistics analysis on the particle size distribution and particle distances is performed for the entire NMC electrode and is used to create the representative volume element (RVE). The RVE is a volume of heterogeneous objects representative to the geometric features of the entire electrode and
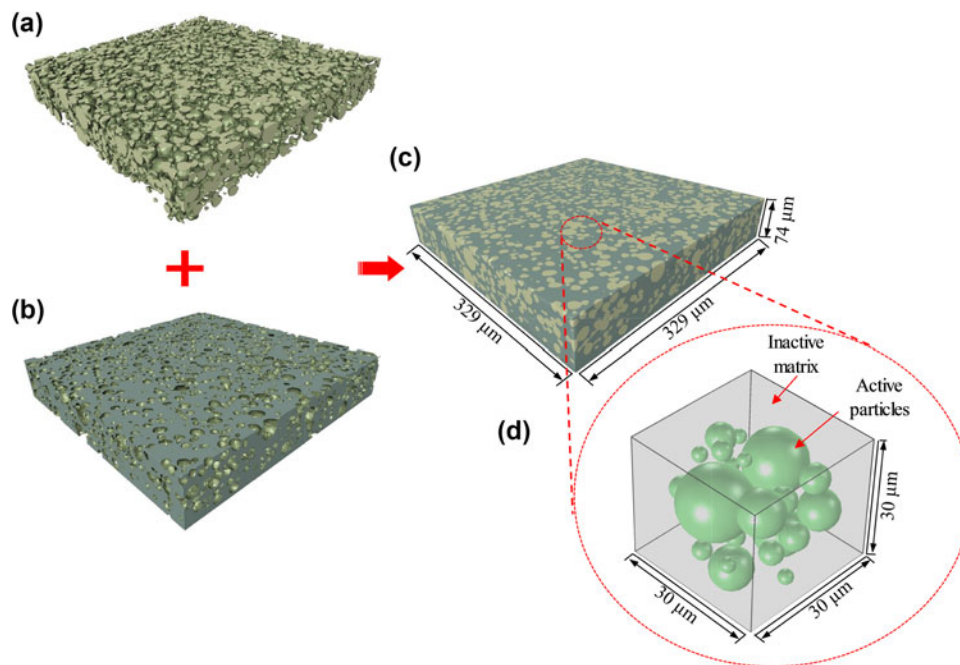
FIG. 2. Reconstruction of NMC composite electrodes. The electrodes are serial-sectioned and 2D images from each layer are aligned, segmented, and stacked into 3D configurations. (a) Active spheroidal NMC particles. (b) Inactive matrix. (c) Reconstructed NMC electrodes composed of active particles and inactive matrix ($329 \times 329 \times 74$ μm^3). (d) RVE of the reconstructed NMC electrode ($30 \times 30 \times 30$ μm^3), where the green spheres represent the active materials and the grey medium represents the inactive components. Li diffuse in the active particles and the surrounding matrix provides mechanical confinement to the deformation of the active materials.

affords the balance between the computational cost and statistical accuracy.[60,61] For NMC, we choose a RVE with the size of $30 \times 30 \times 30$ μm^3 that contains 27 particles, Fig. 2(d). The particles are spherical in nature as is observed in the majority of the particles of the reconstructed electrode (7752 particles). As stated earlier, the details of the microstructure determine the stress field and the electrochemical behaviors of the composite electrodes. We carefully compare the statistical features of the RVE versus the entire reconstructed volume. Figure 3(a) shows the particle size distribution. The probability is calculated by the sum of the volumes of the particles within a given size interval divided by the total volume of all the particles. Figures 3(b) and 3(c) show the distance (surface to surface) of the nearest neighbors and the average and standard deviation of the distance from the 1st, 2nd, and 3rd neighbors for individual particles, respectively. The statistical analysis of the RVE for the NMC electrode compressed by 2000 bar after fabrication is shown in Fig. S1 in the Supplementary Material. In addition, Table I provides further information on the volume fraction of the active particles V_f, the average diameter of the particles A, as well as the number of particles in the RVEs of uncompressed/compressed samples. The selected RVEs indeed show the same statistical features of the entire NMC electrodes and thus are representative to microstructure of the composite electrodes.

In another sample, we choose the SnO electrode as a representative of high-capacity electrodes that undergoes large elasto-plastic deformation upon lithiation. Figure 4(a) shows the scanning electron microscopy (SEM) image of the SnO particles with an estimated average diameter of 30 μm. The reconstructed model [$682 \times 747 \times 84$ μm^3, Fig. 4(b)] shows that a large portion of the particles have irregular shapes and particles in local regions are aggregated. The complexity of particle geometries places a challenge in the selection of the RVE. We choose a local collection of the SnO particles and adjust the size the RVE to ensure that the volume fraction of the active particles is close to that in the entire electrode. Figure 4(c) shows the RVE which has rough particle surfaces, aggregated particles, and initial defects of voids and cracks. To avoid the computational singularity, we utilize the Laplacian smoothing method to smooth the particle surface and delete those structural defects. The RVE after surface smoothing has a size of $50 \times 50 \times 35$ μm^3 and the mesh is shown in Fig. 4(d). Albeit relatively small size, the RVE is a reasonable representation of the microstructural feature of the SnO electrodes.

IV. RESULTS AND DISCUSSION

NMC is a class of cathode materials attractive for the application of electric vehicles. We take the NMC as an
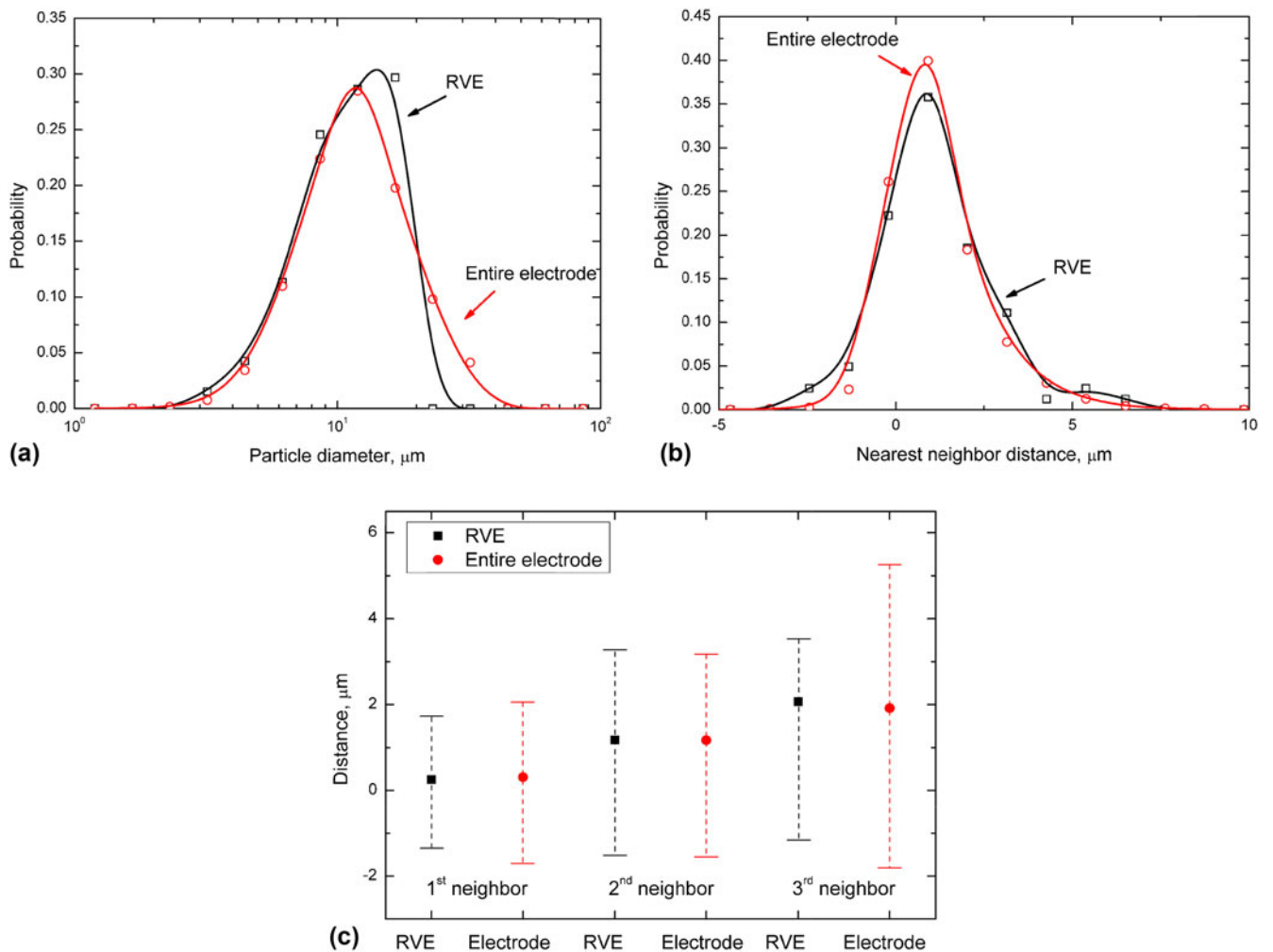
FIG. 3. Statistical analysis of RVE in comparison with the reconstructed entire NMC electrode. (a) Particle size distribution. (b) Probability distribution of the distance from the nearest neighbor for individual particles. (c) The average and standard deviation of the distance from the 1st, 2nd, and 3rd neighbors for individual particles in the reconstructed NMC electrodes (red) and in the RVE (black).

TABLE I. Statistic data for the NMC electrodes and RVEs.

	Uncompressed RVE	Uncompressed NMC electrode	Compressed RVE	Compressed NMC electrode
Volume fraction V_f, %	27.03	26.85	38.74	38.62
Average radius A, μm	3.08	3.03	3.08	2.78
Number of particles	27	7752	27	13,993

example to examine the mechanical behaviors of intercalation-type electrodes which usually undergo relatively small volumetric strain upon lithiation (<10%). In the numerical modeling, we have assumed a perfect bonding between the active particles and the inactive matrix. The stress field in the composite electrode is induced by the coexistence of inhomogeneous distribution of Li and thus mismatch strains in the active particles, the mechanical confinement of the matrix against the volumetric change of the particles, and the contact of neighboring particles. Li distribution and

the stress field dynamically co-evolve because of the coupling effect of diffusion and stresses. The radii of the NMC particles vary from 1.49 μm to 7.67 μm with an average value of $A = 3.08$ μm. The size of the matrix for the uncompressed sample is $30 \times 30 \times 30$ μm^3, and its size in the compressed sample decreases to $30 \times 30 \times 21$ μm^3 while the volume of the active particles remains the same. The material properties are adopted as follows. For NMC, elastic constitutive behavior is adopted and the mechanical properties are considered to be independent of the Li composition.
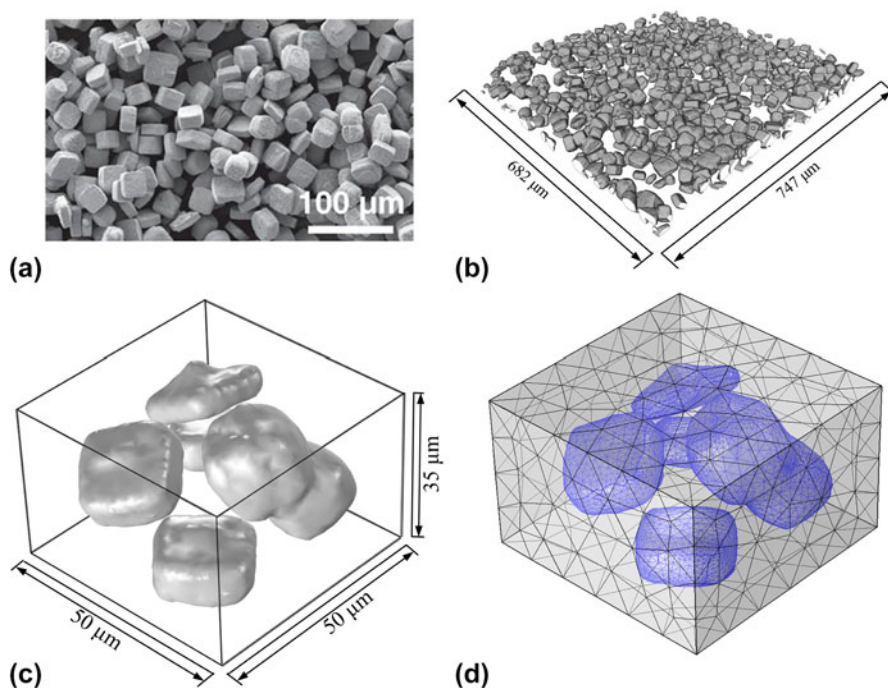
FIG. 4. Reconstruction of SnO composite electrodes. (a) SEM image of SnO particles. Reproduced with permission from Ebner el al. *Science*, 342, 716, 2013, by the American Association for the Advancement of Science. (b) 3D visualization of reconstructed SnO particles ($682 \times 747 \times 85$ μm³). (c) RVE of the reconstructed SnO electrode ($50 \times 50 \times 35$ μm³). (d) Mesh of the SnO RVE after surface smoothing.

We set the Young's modulus $E_{NMC} = 120$ GPa,[41] Poisson's ratio $v_{NMC} = 0.3$, Li diffusivity $D = 10^{-15}$ m²/s,[62] partial molar volume of Li in NMC $\Omega = 1.3 \times 10^{-30}$ m³,[63] the activity coefficient $\gamma = 1$, and the temperature $T = 300$ K. The constitutive behavior of inactive matrix is described by a Neo-Hookean material model with the Young's modulus $E = 4.2$ GPa and Poisson's ratio $v = 0.3$.[41] The volumetric strains of NMC materials upon full lithiation are in the range of 4–10%.[63] We set the volumetric strain 9% at the fully lithiated state in the numerical calculations and assume the deformation is linearly proportional to the Li concentration. Therefore, the maximum Li concentration can be calculated as $C_{max} = 0.09/\Omega$. We also systematically vary the volumetric strain to study its influence on the mechanical and electrochemical performance of the electrodes. To model the potentiostatic lithiation process, we set a constant chemical potential μ_S on the surface of active particles which equals to the chemical potential of Li at the fully lithiated state of NMC without the influence of mechanical stresses, $\mu_S = \mu_0 + kT \log(\Omega C_{max}/\det(F))$. For the galvanostatic lithiation, the time φ to reach the theoretical capacity of NMC is used to represent the charging rate. The nominal flux J_0 is then determined through the relationship $V_{NMC}C_{max} = S_{NMC}J_0\varphi$. At the charging rate $\varphi = 1$ h, $J_0 = 5.54 \times 10^{-5}$ mol/m².

The stress field and Li concentration within the composite electrode are solved simultaneously. We demonstrate the evolution of stresses and the mechanical interactions regulated Li transport under the potentiostatic lithiation condition. Figure 5(a) shows the sectional view of Li profiles in the uncompressed RVE at different dimensionless time steps $\bar{t} = Dt/A^2$. As expected, lithiation proceeds at different degrees in the particles of different sizes. Particles of small size are lithiated much faster than those large particles. Within individual particles, Li distribution is highly inhomogeneous where the outer shell region is Li rich and the inner core is Li poor. The gradient of Li concentration induces mismatch strains and generates compressive stresses in the outer shell regions and tension around the inner core. Meanwhile, the expansion of particles is constrained by the inactive matrix as well as neighboring particles, inducing an extra compressive stress field in the particles. The magnitude of this additional compressive stress depends on the Li concentration in the active particles, the size and pattern of the active particles, as well as the mechanical properties of the active and inactive materials. The stresses influence the Li transport in the way that the stress gradient within a particle tends to homogenize the distribution of Li and drives Li diffusion from the compressed region (Li rich) to the tensed side (Li poor).

The inhomogeneity of Li distribution reduces the effective capacity of the composite electrodes. With regard to the stress effect on the capacity, the local compressive stresses increase the chemical potential of Li, impeding the Li insertion and thus reducing the
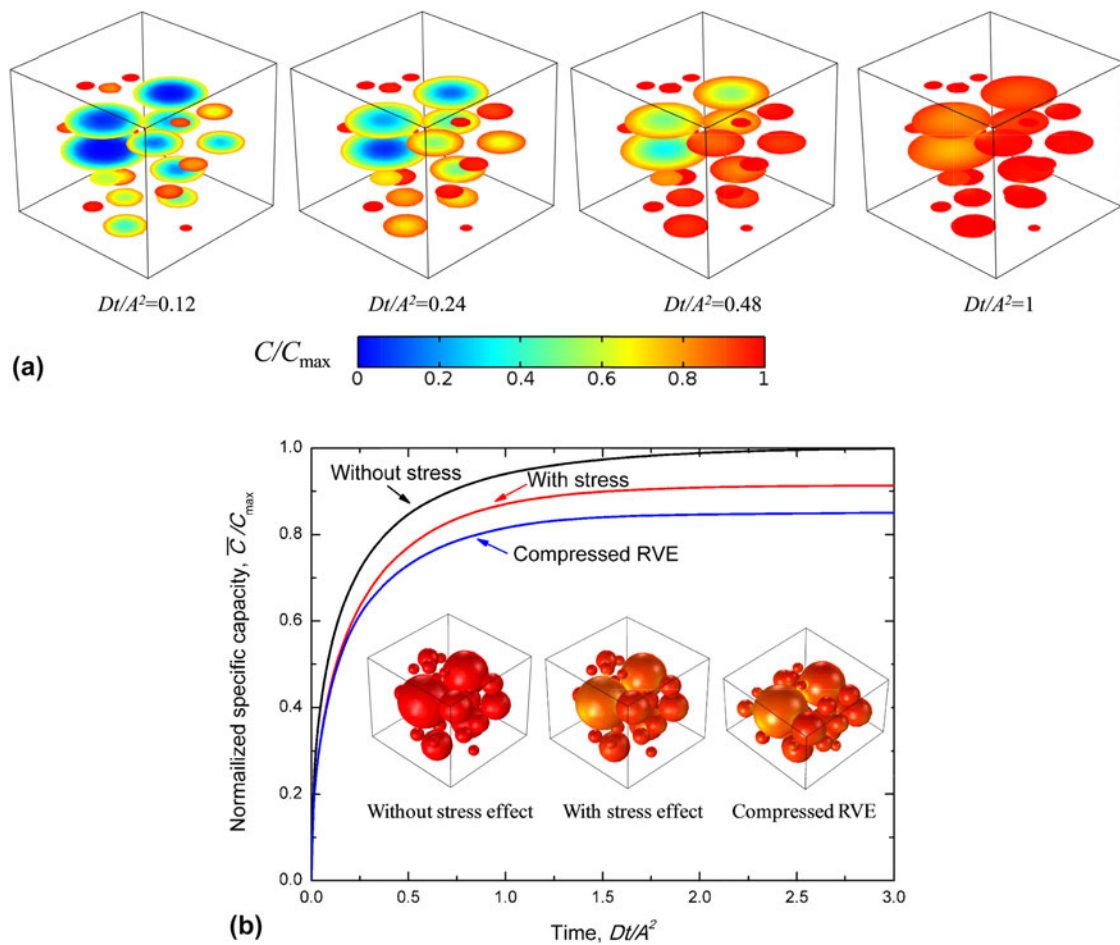
FIG. 5. The effect of mechanical interactions on Li distribution and capacity of the RVE. (a) The sectional view of Li profiles at different time steps during potentiostatic lithiation of the RVE. Li diffusion is driven by both the Li concentration gradient and the stress field. (b) Normalized specific capacity as a function of the lithiation time for the uncompressed RVE with (red line) and without (black line) including the stress effect on diffusion and for the compressed RVE including the stress effect (blue line), respectively. Inset figures show the Li distribution at the fully lithiated state for the three cases.

deliverable capacity. To demonstrate the extent of the stress modulated capacity, we simulate lithiation in three sets of samples: uncompressed RVE with and without including the stress effect on Li diffusion, and compressed RVE with the stress effect. Figure 5(b) plots the normalized specific capacity $\bar{C}/C_{max}$ as a function of the lithiation time in the three cases where $\bar{C}$ represents the average Li concentration over all the NMC particles. The specific capacity increases quickly at the initial stage of lithiation because of the large driving force of chemical potential, and then gradually approach to the steady state. Without considering the stress effect on Li diffusion (black line), the normalized capacity reaches the unit at the fully lithiated state and Li insertion in each single particle is saturated. In comparison, the uncompressed RVE shows a significant loss of capacity ($\sim$10%) at the fully lithiated state if the stress effect on Li diffusion is accounted (red line). For compressed RVE (blue line), the capacity is reduced to an even larger

extent. This is due to the fact that the smaller particle spacing in the compressed samples induces a higher compressive stress filed in both the active particles and the inactive matrix. More discussions about the stress evolution within the particles upon lithiation can be found in our previous work.[51] The inset snapshots in Fig. 5(b) show the Li profiles in the three configurations upon full lithiation. It is evident that Li insertion is blocked in the regions where large compressive stresses develop. Fig. S2 in the Supplementary Material shows the local microstructural details and the correspondence between the Li distribution and mean stresses in the uncompressed RVE without and with the stress effect in comparison with the results of the compressed RVE.

To further examine the compressive stress induced capacity loss, we look into the individual contributions due to the matrix confinement and particles contact. Figure 6(a) plots the distribution of Li concentration along the radius of a particle which is free of contact with
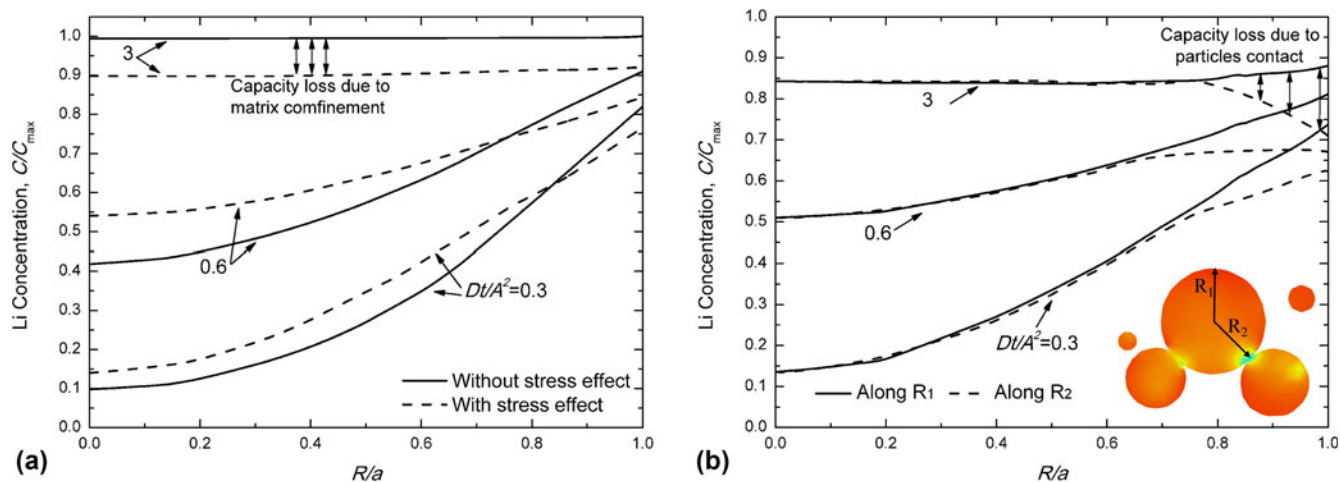
FIG. 6. Capacity loss due to the mechanical confinement of the matrix and particles contact. (a) Radial distribution of Li in a particle which is free of contact with its neighbors. The mechanical confinement is provided only by the matrix. The solid and dashed lines represent the results calculated with and without accounting for the stress effect on Li diffusion, respectively. The compressive stresses developed by the matrix confinement tend to homogenize the Li distribution within the active particles and decrease the effective capacity. (b) Li profiles along two radii of different orientations. R_1 represents the direction along which the particle is free of contact with others, and R_2 represents the direction along which the particle is in contact with its neighbor.

its neighbors. The solid and dashed lines represent the Li profile at different lithiation steps without and with including the stress effect on Li diffusion, respectively. The compressive stresses developed by the mechanical constraint of the inactive matrix smooth the Li concentration gradient in the particle. At the fully lithiated state, the compressive stress exerted on the outer surface of the particle counterbalances the driving force of concentration gradient for Li diffusion and blocks further insertion of Li. The ~10% capacity loss at the terminal state of lithiation is attributed to the mechanical confinement of the matrix. In another particle, Fig. 6(b) plots the Li distribution along two radii, where R_1 represents the direction along which the particle is free of contact with others (solid line), and R_2 represents the direction along which the particle is in contact with its neighbor (dashed line). The difference of Li concentrations along the two orientations represents the capacity loss due to the particles contact. The local contact generates a large magnitude of compressive stresses that cause deficiency of Li storage around the outer regime of the particle. The inhomogeneity of Li profiles also induces anisotropic deformation of the particle that the spherical particle may evolve into nonspherical shapes.

The accessible capacity of the composite electrodes depends on the internal stresses. The stress field in the active particles dynamically evolves in the electrochemical processes of Li insertion and extraction, and is further determined by the geometric features of the particles, the volume fraction of the active materials, the volumetric expansion during lithiation, and the effective properties of the matrix. We screen the specific capacity of the electrodes in terms of the variation of the volume fraction
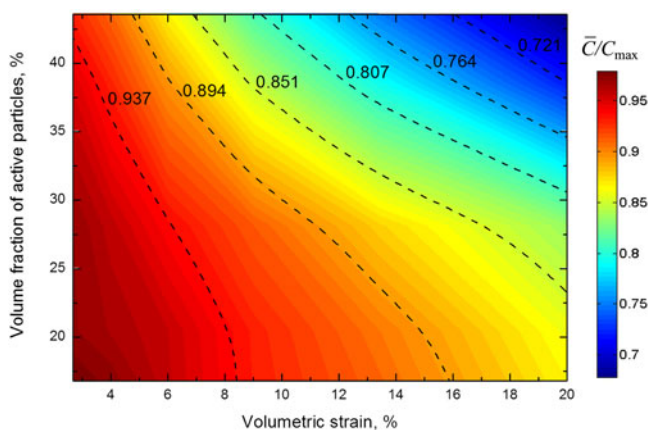

FIG. 7. Contour plot of specific capacity of the composite electrode in terms of the volumetric strain and volume fraction of the active particles. Higher values of the volume fraction and the volumetric strain (upper right region) significantly reduce the effective specific capacity because of the mechanical interactions of the constituent components.

of the active particles V_f and the volumetric strain upon full lithiation ε_V. Figure 7 shows the contour plot of the normalized specific capacity $\bar{C}/C_{max}$. The capacity decrease as V_f and ε_V increase (upper right regime in Fig. 7) because both the higher occupancy and larger deformation of the active material result in severe mechanical interactions among the constituted components which in turn reduce the effective capacity. The dependence on V_f indicates that the effective capacity of the composite electrode is not linearly scaled with the mass of the active material, but is limited by the inhomogeneous storage of Li that is modulated by the mechanical stresses. In terms

of the volumetric strain ε_V, albeit smaller values compared to that in high-capacity electrodes, the stress can still be significant because the active particles are usually ceramic-like materials with high stiffness. In addition to the two studied parameters, the contour plot of capacity can be extended to multi-dimensions by including, for instance, the stiffness ratio of the active and inactive materials, the sphericity of the particles, the distance of neighboring particles, among others. There is a wide spectrum in the design of composite electrodes to reach the optimum electrochemical behaviors and mechanical performance. The computational program provides a viable tool in the selection of materials and design of the geometries of the constituted components. For the interest of different boundary conditions, Fig. S3 in

the Supplementary Material shows the results of galvanostatic lithiation including the specific capacity of the electrodes at different charging rates and the influence of the stress field on the capacity retention. Same conclusion is drawn that the stress field regulates Li transport and large compressive stresses may significantly reduce the capacity of the composite electrodes.

Another important aspect in the design of composite electrodes is to avoid the structural disintegration due to the fracture of the conductive matrix or interfacial debonding between the active material and the matrix. The potential failure can be dictated by the stresses in the matrix. Figures 8(a) and 8(b) show the distribution of the first principal stress and shear stress in a cross section of the inactive matrix at fully lithiated state. The maximum
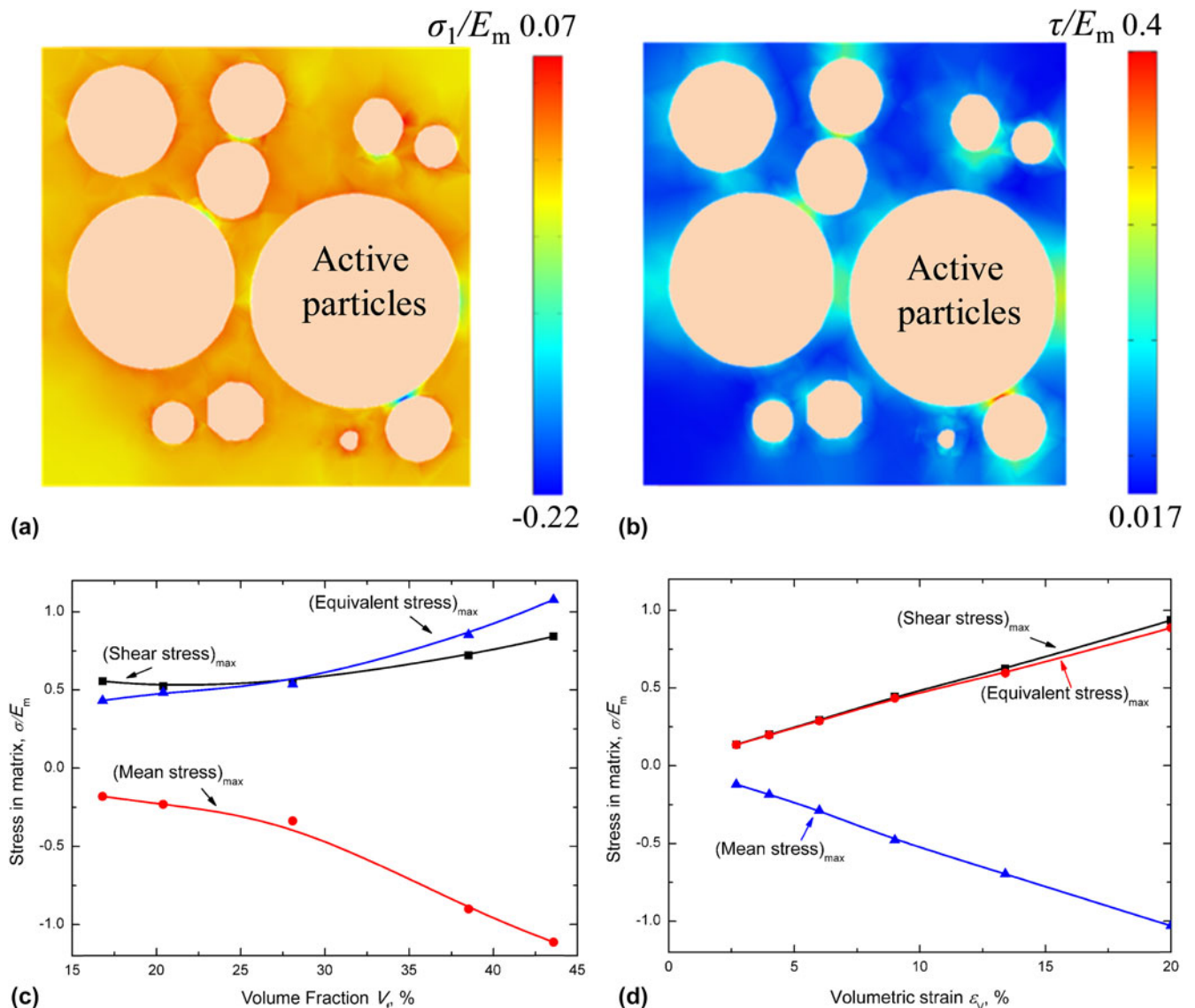

FIG. 8. Plots of (a) the first principal stress and (b) shear stress in the matrix. The regions in between two particles are subject to large stresses that might lead to fracture or debonding of inactive matrix during lithiation. The maximum shear stress, equivalent stress, and mean stress in the matrix as a function of (c) the volume fraction and (d) the volumetric strain of the active particles.

stresses in the matrix are located at the regimes in between the close particles. The normal stress may cause the tear of the polymer matrix or irreversible morphology changes. On the other hand, the shear stress is the major cause of the interfacial debonding between the particles and the matrix. The disconnection of the particle network ultimately isolates the active particles and increases the ohmic and thermal resistance of the electrodes—another known factor that causes persistent capacity loss of the electrodes over cycles. Figures 8(c) and 8(d) plot the quantitative characterization of the stresses (maximum shear stress, equivalent stress, and mean stress) in the matrix as a function of the volume fraction V_f and the volumetric strain ε_V, respectively. The magnitude of the three stress components increases with an almost

proportional relationship with the two variables. In the limiting cases of $V_f = 40\%$ and $\varepsilon_V = 20\%$, the stresses reach the value of the stiffness of the matrix. Such large stresses are hardly sustainable for the polymer matrix. The damage evolution in the matrix will be a topic of interest to be explored in future studies.

Large deformation and geometric nonlinearly are challenging topics in continuum mechanics. To demonstrate the capability of the computational program for the materials experiencing large elasto-plasticity during Li insertion, we investigate mechanical behaviors and stress modulated Li transport in SnO composite electrodes. Metal oxides hold the great promise of high-capacity anodes to replace the conventional graphite materials. Most studies on metal oxides have been focused on
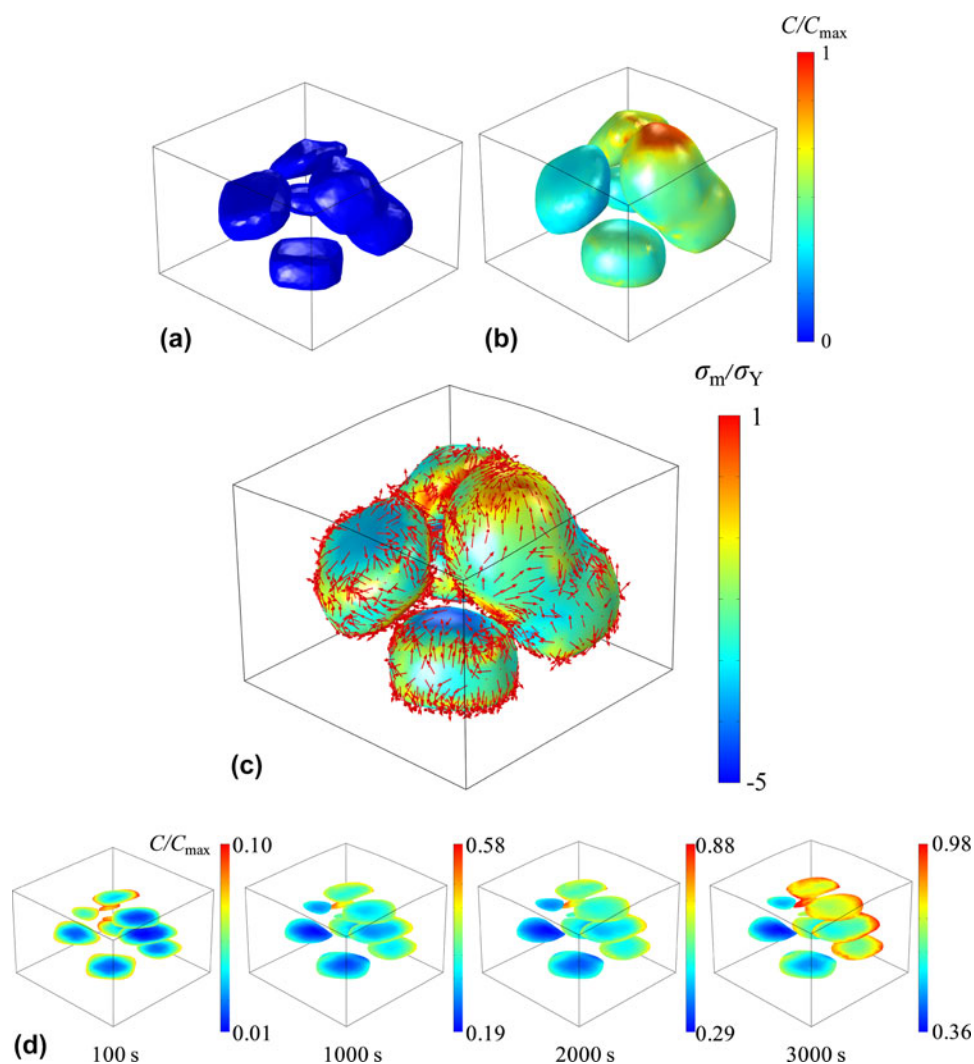

FIG. 9. Li distribution in the SnO particles (a) before lithiation and (b) after galvanostatic lithiation for 1 h. (c) The profiles of mean stresses and Li flux within the particles. The particles are color coded by the magnitude of mean stresses where blue color represents the regimes under large compressive stresses and red color shows the regimes under large tensile stresses. Li flux is represented by the red arrows. It is evident that local tensile stresses attract Li while the compressive stresses drive Li away. (d) Cross-sectional visualization of Li profiles in the reconstructed RVE at different time steps during the galvanostatic lithiation.

their electrochemical performance and the reaction mechanisms. On the mechanical aspect, a large volumetric strain ($\sim$100%) is often associated with the lithiation process in metal oxides that challenges the structural stability in the long-term cycles. However, the mechanical behaviors of oxide electrodes have been rarely explored. We reconstruct the 3D model of SnO composites and import the RVE into the finite element program. Details are described in Sec. III. The material properties for SnO particles are assumed to be constant. We set Young's modulus E_{SnO} = 50 GPa,[64] Poisson's ratio v_{SnO} = 0.3, yield strength σ_Y = 200 MPa,[64] Li diffusivity D = 10^{-13} m^2/s,[65] partial molar volume of Li in SnO Ω = 1.35×10^{-29} m^3,[59] the activity coefficient γ = 1, and the temperature T = 300 K. Experimental results show that the volume strain of SnO is proportional to the lithiation state and reaches 258% upon fully lithiated.[59,66] Therefore, we assume the volume expansion of SnO as a linear function of Li concentration and set the maximum Li concentration C_{max} = 2.6/Ω_{SnO}. We adopt an elastic and perfect plastic constitutive model that SnO particles yield when the equivalent stress reaches the yield strength σ_Y. We simulate the galvanostatic lithiation. The time to reach the theoretical capacity of SnO is set to be φ, and the nominal flux J_0 is determined through the relationship $V_{SnO}C_{max} = S_{SnO}J_0\varphi$. For the lithiation rate φ = 2 h, J_0 = 1.32×10^{-4} mol/m^2.

Different from the spherical NMC particles, the fabricated SnO shows irregular shapes and rough surfaces. The geometric features will influence the Li distribution and determine the stress field. Li tends to accumulate at the regions of smaller surface curvature. Meanwhile, stresses are concentrated at the edges and corners which place a strong driving force of Li diffusion. Figures 9(a) and 9(b) show the Li distribution in the SnO particles before lithiation and after Li insertion for 1 h. It is evident that lithiation in different particles proceeds at different stages. Within individual particles, Li distribution is highly inhomogeneous that Li is concentrated in the bulged regimes of smaller surface curvature. The particles are color coded by the magnitude of the mean stress in Fig. 9(c) and the red arrows show the local Li flux. The local tensile stress attracts Li insertion while compressive stresses drive Li away. Figure 9(d) shows the cross-sectional view of Li profiles in the reconstructed RVE at different time steps. The aggregated particles of irregular shapes show higher concentration of Li because of the effects of both the surface curvature and the mechanical stress. The high disparity of Li concentration over the active particles generally compromises the electrochemical performance of the battery packages. Recent studies[58,67] have also pointed out that the mechanical and electrochemical performance of electrodes can be improved if the active particles are synthesized with the control of size, shape, and alignment.

V. CONCLUSION

The mechanical stresses and electrochemical behaviors of Li-ion batteries are intimately coupled. While the mechanical failure of batteries is well recognized in the research community, the stress regulated Li transport and thus the deliverable capacity of batteries have been overlooked. The dynamic nature of mechanical interactions in the heterogeneous composite electrodes adds a further challenge in characterizing the stress effect. We develop a finite element program that computes coupled Li diffusion and stresses for three-dimensional composite electrodes. We employ the reconstructed models for commercial batteries to study the co-evolution of stresses and Li storage. The NMC cathode represents the intercalation-type electrodes of spherical shape and small deformation, while the SnO anode represents the high-capacity materials of irregular shapes and dramatic volumetric change upon Li insertion. The state of charge in the percolated active particles is highly inhomogeneous regulated by the stress field. Significant capacity loss is possible due to the mechanical confinement of the inactive matrix and particles contact. A multi-dimensional space of design is open for the optimization of the mechanical and electrochemical performance of composite electrodes by the selection of the geometry, network, and properties of the active particles and the surrounding medium.

ACKNOWLEDGMENTS

REFERENCES

1. M. Armand and J.M. Tarascon: Building better batteries. *Nature* **451**, 652 (2008).
2. M.S. Whittingham: Materials challenges facing electrical energy storage. *MRS Bull.* **33**, 411 (2008).
3. J.M. Tarascon and M. Armand: Issues and challenges facing rechargeable lithium batteries. *Nature* **414**, 359 (2001).
4. B. Scrosati and J. Garche: Lithium batteries: Status, prospects and future. *J. Power Sources* **195**, 2419 (2010).
5. N. Nitta, F. Wu, J.T. Lee, and G. Yushin: Li-ion battery materials: Present and future. *Mater. Today* **18**, 252 (2015).
6. A. Mukhopadhyay and B.W. Sheldon: Deformation and stress in electrode materials for Li-ion batteries. *Prog. Mater. Sci.* **63**, 58 (2014).
7. M.T. McDowell, S. Xia, and T. Zhu: The mechanics of large-volume-change transformations in high-capacity battery materials. *Extreme Mech. Lett.* (2016). doi: 10.1016/j.eml.2016.03.004.
8. J. Christensen and J. Newman: A mathematical model of stress generation and fracture in lithium manganese oxide. *J. Electrochem. Soc.* **153**, A1019 (2006).

9. M.M. Thackeray: Structural considerations of layered and spinel lithiated oxides for lithium ion batteries. *J. Electrochem. Soc.* **142**, 2558 (1995).

10. V. Malavé, J.R. Berger, H. Zhu, and R.J. Kee: A computational model of the mechanical behavior within reconstructed Li_xCoO_2 Li-ion battery cathode particles. *Electrochim. Acta* **130**, 707 (2014).

11. K. Zaghib, C.M. Julien, and J. Prakash: *Proceedings of the International Symposium: New trends in intercalation compounds for energy storage and conversion* (The Electrochemical Society, Pennington, 2003).

12. I.A. Courtney and J.R. Dahn: Electrochemical and in situ x-ray diffraction studies of the reaction of lithium with tin oxide composites. *J. Electrochem. Soc.* **144**, 2045 (1997).

13. K. Zhao, M. Pharr, J.J. Vlassak, and Z. Suo: Fracture of electrodes in lithium-ion batteries caused by fast charging. *J. Appl. Phys.* **108**, 073517 (2010).

14. X.H. Liu, L. Zhong, S. Huang, S.X. Mao, T. Zhu, and J.Y. Huang: Size-dependent fracture of silicon nanoparticles during lithiation. *ACS Nano* **6**, 1522 (2012).

15. J.W. Choi, Y. Cui, and W.D. Nix: Size-dependent fracture of Si nanowire battery anodes. *J. Mech. Phys. Solids* **59**, 1717 (2011).

16. K. Zhao, M. Pharr, L. Hartle, J.J. Vlassak, and Z. Suo: Fracture and debonding in lithium-ion batteries with electrodes of hollow core–shell nanostructures. *J. Power Sources* **218**, 6 (2012).

17. S.W. Lee, H.W. Lee, W.D. Nix, H. Gao, and Y. Cui: Kinetics and fracture resistance of lithiated silicon nanostructure pairs controlled by their mechanical interaction. *Nat. Commun.* **6**, 7533 (2015).

18. K. Zhao, W.L. Wang, J. Gregoire, M. Pharr, and Z. Suo: Lithium-assisted plastic deformation of silicon electrodes in lithium-ion batteries: A first-principles theoretical study. *Nano Lett.* **11**, 2962 (2011).

19. K. Zhao, G.A. Tritsaris, M. Pharr, W.L. Wang, O. Okeke, Z. Suo, J.J. Vlassak, and E. Kaxiras: Reactive flow in silicon electrodes assisted by the insertion of lithium. *Nano Lett.* **12**, 4397 (2012).

20. L. Brassart and Z. Suo: Reactive flow in solids. *J. Mech. Phys. Solids* **61**, 61 (2013).

21. J.W. Choi, J. McDonough, S. Jeong, J.S. Yoo, C.K. Chan, and Y. Cui: Stepwise nanopore evolution in one-dimensional nanostructures. *Nano Lett.* **10**, 1409 (2010).

22. X.H. Liu, S. Huang, S.T. Picraux, J. Li, T. Zhu, and J.Y. Huang: Reversible nanopore formation in Ge nanowires during lithiation–delithiation cycling: An in situ transmission electron microscopy study. *Nano Lett.* **11**, 3991 (2011).

23. K. Zhao, M. Pharr, Q. Wan, W.L. Wang, E. Kaxiras, J.J. Vlassak, and Z. Suo: Concurrent reaction and plasticity during initial lithiation of crystalline silicon in lithium-ion batteries. *J. Electrochem. Soc.* **159**, A238 (2012).

24. M.T. McDowell, S.W. Lee, C. Wang, W.D. Nix, and Y. Cui: Studying the kinetics of crystalline silicon nanoparticle lithiation with in situ transmission electron microscopy. *Adv. Mater.* **24**, 6034 (2012).

25. H. Yang, W. Liang, X. Guo, C.M. Wang, and S. Zhang: Strong kinetics-stress coupling in lithiation of Si and Ge anodes. *Extreme Mech. Lett.* **2**, 1 (2015).

26. G. Sandu, L. Brassart, J.F. Gohy, T. Pardoen, S. Melinte, and A. Vlad: Surface coating mediated swelling and fracture of silicon nanowires during lithiation. *ACS Nano* **8**, 9427 (2014).

27. M.W. Verbrugge and B.J. Koch: Modeling lithium intercalation of singlefiber carbon microelectrodes. *J. Electrochem. Soc.* **143**, 600 (1996).

28. J. Christensen and J. Newman: Stress generation and fracture in lithium insertion materials. *J. Solid State Electrochem.* **10**, 293 (2006).

29. X. Zhang, W. Shyy, and A.M. Sastry: Numerical simulation of intercalation-induced stress in Li-ion battery electrode particles. *J. Electrochem. Soc.* **154**, A910 (2007).

30. Y.T. Cheng and M.W. Verbrugge: Evolution of stress within a spherical insertion electrode particle under potentiostatic and galvanostatic operation. *J. Power Sources* **190**, 453 (2009).

31. S. Golmon, K. Maute, S.H. Lee, and M.L. Dunn: Stress generation in silicon particles during lithium insertion. *Appl. Phys. Lett.* **97**, 033111 (2010).

32. H. Haftbaradaran, X. Xiao, M.W. Verbrugge, and H. Gao: Method to deduce the critical size for interfacial delamination of patterned electrode structures and application to lithiation of thin-film silicon islands. *J. Power Sources* **206**, 357 (2012).

33. Y. Gao and M. Zhou: Strong stress-enhanced diffusion in amorphous lithium alloy nanowire electrodes. *J. Appl. Phys.* **109**, 014310 (2011).

34. A.F. Bower, P.R. Guduru, and V.A. Sethuraman: A finite strain model of stress, diffusion, plastic flow, and electrochemical reactions in a lithium-ion half-cell. *J. Mech. Phys. Solids* **59**, 804 (2011).

35. L. Brassart, K. Zhao, and Z. Suo: Cyclic plasticity and shakedown in high-capacity electrodes of lithium-ion batteries. *Int. J. Solids Struct.* **50**, 1120 (2013).

36. Z. Cui, F. Gao, and J. Qu: A finite deformation stress-dependent chemical potential and its applications to lithium ion batteries. *J. Mech. Phys. Solids* **60**, 1280 (2012).

37. H. Yang, S. Huang, X. Huang, F. Fan, W. Liang, X.H. Liu, L.Q. Chen, J.Y. Huang, J. Li, T. Zhu, and S. Zhang: Orientation-dependent interfacial mobility governs the anisotropic swelling in lithiated silicon nanowires. *Nano Lett.* **12**, 1953 (2012).

38. H. Yang, F. Fan, W. Liang, X. Guo, T. Zhu, and S. Zhang: A chemo-mechanical model of lithiation in silicon. *J. Mech. Phys. Solids* **70**, 349 (2014).

39. Z. Jia and T. Li: Stress-modulated driving force for lithiation reaction in hollow nano-anodes. *J. Power Sources* **275**, 866 (2015).

40. Z. Jia and T. Li: Intrinsic stress mitigation via elastic softening during two-step electrochemical lithiation of amorphous silicon. *J. Mech. Phys. Solids* **91**, 278 (2016).

41. L.S. de Vasconcelos, R. Xu, J. Li, and K. Zhao: Grid indentation analysis of mechanical properties of composite electrodes in Li-ion batteries. *Extreme Mech. Lett.* (2016). doi: 10.1016/j.eml.2016.03.002.

42. T. Hutzenlaub, S. Thiele, R. Zengerle, and C. Ziegler: Three-dimensional reconstruction of a $LiCoO_2$ Li-ion battery cathode. *Electrochem. Solid-State Lett.* **15**, A33 (2011).

43. T. Hutzenlaub, S. Thiele, N. Paust, R. Spotnitz, R. Zengerle, and C. Walchshofer: Three-dimensional electrochemical Li-ion battery modelling featuring a focused ion-beam/scanning electron microscopy based three-phase reconstruction of a $LiCoO_2$ cathode. *Electrochim. Acta* **115**, 131 (2014).

44. M. Ebner and V. Wood: Tool for tortuosity estimation in lithium ion battery porous electrodes. *J. Electrochem. Soc.* **162**, A3064 (2015).

45. C. Lim, B. Yan, L. Yin, and L. Zhu: Simulation of diffusion-induced stress using reconstructed electrodes particle structures generated by micro/nano-CT. *Electrochim. Acta* **75**, 279 (2012).

46. M.D. Chung, J.H. Seo, X.C. Zhang, and A.M. Sastry: Implementing realistic geometry and measured diffusion coefficients into single particle electrode modeling based on experiments with single $LiMn_2O_4$ spinel particles. *J. Electrochem. Soc.* **158**, A371 (2011).

47. J. Hun, M. Chung, M. Park, S. Woo, X. Zhang, and A. Marie: Generation of realistic particle structures and simulations of internal stress: A numerical/AFM study of $LiMn_2O_4$ particles. *J. Electrochem. Soc.* **158**, A434 (2011).

48. S.A. Roberts, V.E. Brunini, K.N. Long, and A.M. Grillet: A framework for three-dimensional mesoscale modeling of anisotropic swelling and mechanical deformation in lithium-ion electrodes. *J. Electrochem. Soc.* **161**, F3052 (2014).

49. H. Mendoza, S.A. Roberts, V.E. Brunini, and A.M. Grillet: Mechanical and electrochemical response of a LiCoO$_2$ cathode using reconstructed microstructures. *Electrochim. Acta* **190**, 1 (2016).

50. K. Zhao, M. Pharr, S. Cai, J.J. Vlassak, and Z. Suo: Large plastic deformation in high-capacity lithium-ion batteries caused by charge and discharge. *J. Am. Ceram. Soc.* **94** (2011).

51. R. Xu and K. Zhao: Mechanical interactions regulated kinetics and morphology of composite electrodes in Li-ion batteries. *Extreme Mech. Lett.* (2015). doi: 10.1016/j.eml.2015.10.004.

52. M.M. Attard: Finite strain–isotropic hyperelasticity. *Int. J. Solids Struct.* **40**, 4353 (2003).

53. F.C. Larché and J.W. Cahn: Overview no. 41 the interactions of composition and stress in crystalline solids. *Acta Metall.* **33**, 331 (1985).

54. J. Christensen: Modeling diffusion-induced stress in Li-ion cells with porous electrodes. *J. Electrochem. Soc.* **157**, A366 (2010).

55. G.H. Kim, K. Smith, K.J. Lee, S. Santhanagopalan, and A. Pesaran: Multi-domain modeling of lithium-ion batteries encompassing multi-physics in varied length scales. *J. Electrochem. Soc.* **158**, A955 (2011).

56. A. Salvadori, D. Grazioli, and M.G.D. Geers: Governing equations for a two-scale analysis of Li-ion battery cells. *Int. J. Solids Struct.* **59**, 90 (2015).

57. Comsol: Comsol Multiphysics: Version 4.4. (2013).

58. M. Ebner, F. Geldmacher, F. Marone, M. Stampanoni, and V. Wood: X-ray tomography of porous, transition metal oxide based lithium ion battery electrodes. *Adv. Energy Mater.* **3**, 845 (2013).

59. M. Ebner, F. Marone, M. Stampanoni, and V. Wood: Visualization and quantification of electrochemical and mechanical degradation in Li ion batteries. *Science* **342**, 716 (2013).

60. J. Joos, T. Carraro, A. Weber, and E. Ivers-Tiffée: Reconstruction of porous electrodes by FIB/SEM for detailed microstructure modeling. *J. Power Sources* **196**, 7302 (2011).

61. P.R. Shearing, L.E. Howard, P.S. Jørgensen, N.P. Brandon, and S.J. Harris: Characterization of the 3-dimensional microstructure of a graphite negative electrode from a Li-ion battery. *Electrochem. Commun.* **12**, 374 (2010).

62. Y. Wei, J. Zheng, S. Cui, X. Song, Y. Su, W. Deng, Z. Wu, X. Wang, W. Wang, M. Rao, Y. Lin, C. Wang, K. Amine, and F. Pan: Kinetics tuning of Li-ion diffusion in layered Li(Ni$_x$Mn$_y$Co$_z$)O$_2$. *J. Am. Chem. Soc.* **137**, 8364 (2015).

63. Y. Koyama, I. Tanaka, H. Adachi, Y. Makimura, and T. Ohzuku: Crystal and electronic structures of superstructural Li$_{1-x}$[Co$_{1/3}$Ni$_{1/3}$Mn$_{1/3}$]O$_2$ ($0 \leq x \leq 1$). *J. Power Sources* **119**, 644 (2003).

64. N. Qaiser, Y.J. Kim, C.S. Hong, and S.M. Han: Numerical modeling of fracture-resistant Sn micropillars as anode for lithium ion batteries. *J. Phys. Chem. C* **120**, 6953 (2016).

65. M. Winter and J.O. Besenhard: Electrochemical lithiation of tin and tin-based intermetallics and composites. *Electrochim. Acta* **45**, 31 (1999).

66. I.A. Courtney and J.R. Dahn: Electrochemical and in situ x-ray diffraction studies of the reaction of lithium with tin oxide composites. *J. Electrochem. Soc.* **144**, 2045 (1997).

67. R.E. Garcıa, Y.M. Chiang, W.C. Carter, P. Limthongkul, and C.M. Bishop: Microstructural modeling and design of rechargeable lithium-ion batteries. *J. Electrochem. Soc.* **152**, A255 (2005).

Supplementary Material

To view supplementary material for this article, please visit http://dx.doi.org/10.1557/jmr.2016.302.